Unveiling Three Types of Fermions in a Nodal Ring Topological Semimetal through Magneto-Optical Transitions

Jiwon Jeon,[1,*] Taehyeok Kim,[2,*] Jiho Jang,[2] Hoil Kim,[3,4] Mykhaylo Ozerov,[5] Jun Sung Kim,[3,4] Hongki Min,[2,†] and Eunjip Choi[1,‡]

[1]Physics Department, University of Seoul, Seoul 02504, Korea
[2]Department of Physics and Astronomy, Seoul National University, Seoul 08826, Korea
[3]Center for Artificial Low Dimensional Electronic Systems, Institute for Basic Science (IBS), Pohang 37673, Korea
[4]Department of Physics, Pohang University of Science and Technology (POSTECH), Pohang 37673, Korea
[5]National High Magnetic Field Laboratory, Tallahassee, Florida 32310, USA

(Received 12 February 2025; revised 23 June 2025; accepted 22 July 2025; published 19 August 2025)

We investigate the quasiparticles of a single nodal ring semimetal $SrAs_3$ through axis-resolved magneto-optical measurements. We observe three types of Landau levels scaling as $\varepsilon \sim \sqrt{B}$, $\varepsilon \sim B^{2/3}$, and $\varepsilon \sim B$ that correspond to Dirac, semi-Dirac, and classical fermions, respectively. Through theoretical analysis, we identify the distinct origins of these three types of fermions present within the nodal ring. In particular, semi-Dirac fermions—a novel type of fermion that can give rise to a range of unique quantum phenomena —emerge from the end points of the nodal ring where the energy band disperses linearly along one direction and quadratically along the perpendicular direction, a feature not achievable in nodal point or line structures. The capacity of the nodal ring to simultaneously host multiple fermion types, including semi-Dirac fermions, establishes it as a valuable platform to expand the understanding of topological semimetals.

DOI: 10.1103/wfzd-7r9n

Topological semimetals represent a class of materials characterized by conduction and valence bands that cross near the Fermi level. These band crossings, protected by symmetry, result in the formation of nodal points or nodal lines that host exotic quasiparticles, such as Dirac and Weyl fermions. These quasiparticles exhibit novel quantum phenomena, including the chiral anomaly, anomalous Hall effect, and axion electrodynamics [1–3].

Nodal rings are a special form of band-crossing structure. A nodal ring can exhibit, due to its closed and curved geometry, unique quantum phenomena such as Berry flux encirclement, weak antilocalization, and drumhead surface states [4–7]. In particular, a nodal ring can harbor a novel type of fermion, termed the semi-Dirac fermion [8], which acts as Dirac fermions along one direction and classical fermions along the perpendicular direction. This hybrid property of semi-Dirac fermions leads to a range of novel quantum phenomena including exotic non-Fermi liquid states [9], unconventional superconductivity [10], and unusual hydrodynamic transport [11]. However, despite these significant theoretical insights, experimental investigations of nodal ring semimetals are limited compared to those of nodal point and nodal line semimetals.

For probing fermions within topological semimetals, magneto-infrared spectroscopy has proven to be an effective approach. When subjected to a magnetic field, Dirac fermions governed by the linear energy dispersion exhibit Landau levels (LLs) that scale as $\varepsilon \sim \sqrt{B}$, in contrast to

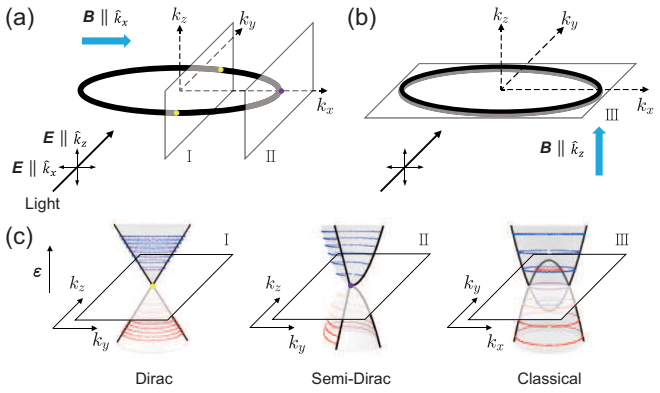

FIG. 1. Schematic diagrams of magneto-optical measurements on a single nodal ring. A magnetic field is applied parallel to k_x and k_z in (a) and (b), respectively. Incident light is polarized along k_x or k_z. (c) Energy dispersions within the three guiding planes I, II, and III shown in (a) and (b), which are linear (I), quadratic (III), and linear + quadratic (II). In (II), the energy bands are cut to illustrate the linear + quadratic dispersions clearly. The blue and red lines represent the LLs with distinct energy spacings, $\varepsilon_n \sim \sqrt{nB}$ for Dirac, $\varepsilon_n \sim [(n+\frac{1}{2})B]^{2/3}$ for semi-Dirac, and $\varepsilon_n \sim (n+\frac{1}{2})B$ for classical fermions, respectively, where n is the LL index.

*These authors contributed equally to this work.
†Contact author: hmin@snu.ac.kr
‡Contact author: echoi@uos.ac.kr

classical fermions with parabolic energy dispersion which display the standard $\varepsilon \sim B$ scaling. Notably, semi-Dirac fermions are predicted to manifest a new type of LL scaling, $\varepsilon \sim B^{2/3}$ due to the hybrid of linear and parabolic energy dispersions [12,13]. The LL scaling can be determined experimentally through the inter-LL optical transitions. While numerous LL transition measurements have been conducted on topological semimetals [14–22], those revealing the signature of semi-Dirac fermions remain sparse [22]. Therefore, the investigations of LL transitions and their corresponding LLs scaling behaviors are critical for unveiling the fermions emerging from a nodal ring.

In this Letter, we perform magneto-infrared measurements on $SrAs_3$. $SrAs_3$ is a recently identified nodal ring semimetal possessing two key features that make it particularly well suited for optical studies [4,5,23,24]. First, $SrAs_3$ features only a single nodal ring within the Brillouin zone (BZ), and second, its low-energy optical transitions arise solely from nontrivial bands, without interference from topologically trivial bands [5,24,25]. The single nodal ring structure of $SrAs_3$ enables controlled alignment of the magnetic field $\boldsymbol{B}$ and the electric field $\boldsymbol{E}$ of incident light along specific directions, such as parallel or perpendicular to the nodal ring axis. This capability allows direction-resolved measurements of LL transitions, thus facilitating a comprehensive investigation of the fermions inherent in the nodal ring.

We reveal that LLs with the novel $\varepsilon \sim B^{2/3}$ scaling emerge in $SrAs_3$, demonstrating the presence of semi-Dirac fermions in the nodal ring. Additionally, we observe two other LLs scaling as $\varepsilon \sim B^{1/2}$ and $\varepsilon \sim B$, arising from Dirac and classical fermions, respectively. We perform a theoretical analysis of the LLs and identify the origins of the three types of fermions. The coexistence of these three types of fermions represents a unique property of the nodal ring, distinguishing it from nodal point or line structures.

Single crystals of $SrAs_3$ were grown using the Bridgman method and their structural, transport, and electron band properties were extensively characterized [4]. The optical reflectivity of $SrAs_3$ was measured at zero magnetic field, and the corresponding optical transitions were theoretically analyzed in Ref. [26]. The magneto-optical measurements were performed under Voigt geometry at $T = 4.2$ K. Broadband reflectances $R(B)$ were taken from $B = 0$ up to 17.45 T over the far- and midinfrared ranges (7–400 meV) using a Fourier transform spectrometer and a bolometric detector.

Figure 1 illustrates the schematic configuration of magneto-optical measurements on a single nodal ring, including the directions of the magnetic field and light polarization. In Fig. 1(a), a magnetic field is applied along $\boldsymbol{B}\|\hat{\boldsymbol{k}}_x$ which is parallel to the nodal ring plane. Incident light propagates along the k_y direction with the electric field $\boldsymbol{E}$ polarized along $\boldsymbol{E}\|\hat{\boldsymbol{k}}_x$ or $\boldsymbol{E}\|\hat{\boldsymbol{k}}_z$. In Fig. 1(b), the magnetic field is applied perpendicular to the nodal ring plane, $\boldsymbol{B}\|\hat{\boldsymbol{k}}_z$. These combinations of $\boldsymbol{B}$ and $\boldsymbol{E}$ yield four kinds of measurement modes, $(\boldsymbol{B},\boldsymbol{E})\|(\hat{\boldsymbol{k}}_z,\hat{\boldsymbol{k}}_z)$, $(\hat{\boldsymbol{k}}_x,\hat{\boldsymbol{k}}_z)$, $(\hat{\boldsymbol{k}}_z,\hat{\boldsymbol{k}}_x)$, and $(\hat{\boldsymbol{k}}_x,\hat{\boldsymbol{k}}_x)$. Further details of the optical measurements are described in Fig. S1 of Supplemental Material (SM), Sec. I [27]. In Figs. 1(a) and 1(b), we introduce three guiding planes I, II, and III that cross the nodal ring to visualize the energy band dispersions within them. These dispersions are linear (I), quadratic (III), and linear along one direction while quadratic along the perpendicular direction (II), as shown in Fig. 1(c). These three types of band structures are derived from a model Hamiltonian of the nodal ring, which will be described later in the theory section.

Figure 2 shows the results of optical reflectance measurements for the two $(\boldsymbol{B},\boldsymbol{E})$ modes with $\boldsymbol{E}\|\hat{\boldsymbol{k}}_z$, i.e, $(\boldsymbol{B},\boldsymbol{E})\|(\hat{\boldsymbol{k}}_x,\hat{\boldsymbol{k}}_z)$, and $(\hat{\boldsymbol{k}}_z,\hat{\boldsymbol{k}}_z)$ In the normalized reflectance $R(B)/R(B=0)$, multiple LL transitions emerge and evolve as B is applied (see SM, Sec. I). To enhance the visibility of the LL transitions, we plot the derivative of the normalized reflectance in Fig. 2. In the $(\boldsymbol{B},\boldsymbol{E})\|(\hat{\boldsymbol{k}}_x,\hat{\boldsymbol{k}}_z)$ mode, two classes of LL transitions, labeled as peaks A and B, are observed. In peak A (orange), LL transitions evolve within the 40–120 meV ranges as B is increased. In contrast, the LL transitions of peak B (black) appear at significantly lower energy ranges, indicating distinct origins of peaks A and B. For the $(\boldsymbol{B},\boldsymbol{E})\|(\hat{\boldsymbol{k}}_z,\hat{\boldsymbol{k}}_z)$ mode, two classes of LL transitions, peak C and peak dCES, where dCES represents the disconnected constant energy surface as will be described later, are observed. The LL transitions of peak C (golden) decrease as B increases, contrary to peaks A and B. The LL transitions of peak dCES (blue) emerge at relatively lower energy ranges below 40 meV.

To elucidate the origins of the four classes of LL transitions, peaks A–C and peak dCES, we perform a theoretical analysis of the magneto-optical transitions of $SrAs_3$. $SrAs_3$ is characterized by an elliptical nodal ring formed around the Y point in the BZ. Optical transitions near the Fermi energy are confined to this nodal ring, enabling the derivation of magneto-optical conductivity using an effective Hamiltonian [26] as

$$H = f_0\sigma_0 s_0 + f_1\sigma_1 s_0 + \hbar v_z k_z \sigma_2 s_0 + \Delta_{\mathrm{SOC}}\sigma_3 s_3, \quad (1)$$

where $f_0 = a_0 + a_x k_x^2 + a_{xy}k_x k_y + a_y k_y^2 + a_z k_z^2$ and $f_1 = b_0 + b_x k_x^2 + b_{xy}k_x k_y + b_y k_y^2 + b_z k_z^2$. The orbital and spin degrees of freedom are represented by Pauli matrices $\boldsymbol{\sigma}$ and $\boldsymbol{s}$, respectively. The nodal ring is located where $k_z = 0$ and $f_1 = 0$, with its axis aligned along the k_z direction. The first term describes the energy tilt that shifts the energy of the nodal ring by f_0, and the last term accounts for SOC (spin-orbit coupling) opening an energy gap of $2\Delta_{\mathrm{SOC}}$, respectively. Further details of Eq. (1) are described in SM, Sec. II [27].

To develop a qualitative understanding of the LL transitions, we first consider a simplified form of Eq. (1), neglecting the effects of tilt, SOC, and ellipticity:

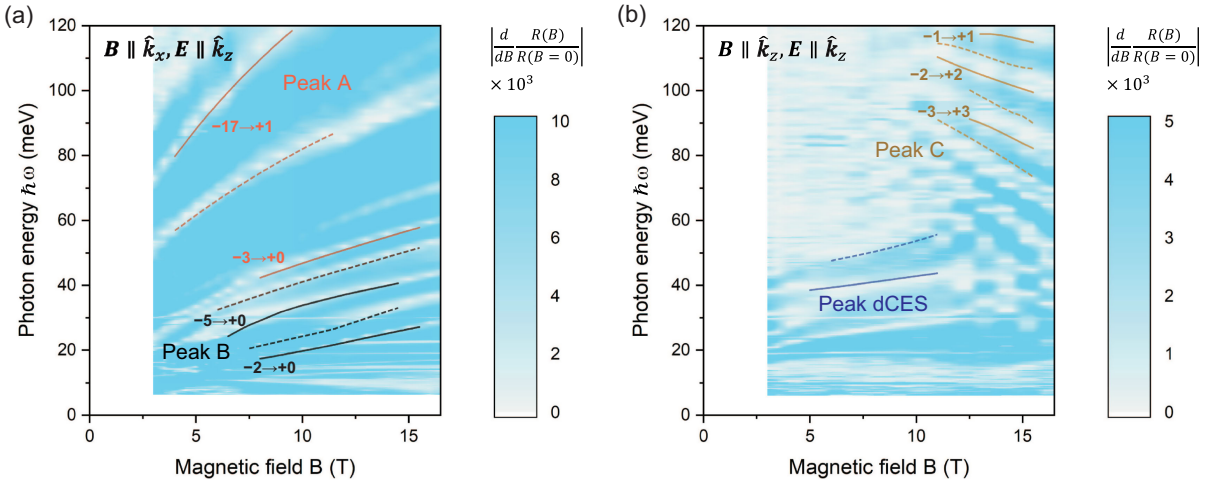

FIG. 2. Experimental magneto-optical transition peaks measured in the (a) $(\boldsymbol{B},\boldsymbol{E})\|(\hat{\boldsymbol{k}}_x,\hat{\boldsymbol{k}}_z)$ mode and (b) $(\boldsymbol{B},\boldsymbol{E})\|(\hat{\boldsymbol{k}}_z,\hat{\boldsymbol{k}}_z)$ mode. The derivative of reflectance ratio $|(d/dB)[R(B)/R(B=0)]|$ was employed in the 2D color plot to enhance visibility. The solid lines represent the regions exhibiting characteristic LL transition peaks corresponding to peaks A–C and peak dCES, while the corresponding dashed lines in between represent dips rather than peaks. The LL indices involved in the optical transitions are labeled, as shown in SM, Fig. S8(a) for peak A, Fig. S8(b) for peak B, and Fig. S4(a) for peak C [27]. For peak A, several LL transitions are involved for each peak, and we assigned representative LL indices, as shown in Fig. S14. The LL-transition peaks were extracted from $(d/dB)[R(B)/R(B=0)]$, except for peak C, which was extracted from the maximum of $[R(B)/R(B=0)]$ due to the monotonic increase in reflectivity level with magnetic field, as explained in detail in SM, Sec. I. As a result, the solid lines of peak C show some deviations from the white region in Fig. 2(b).

$$H=\frac{\hbar^2}{2m}(k_x^2+k_y^2-k_0^2)\sigma_1+\hbar v_z k_z\sigma_2, \tag{2}$$

where the scale of momentum and energy are set to the nodal ring radius k_0 and $\varepsilon_0=\hbar^2k_0^2/2m$, respectively.

First, when the magnetic field is oriented perpendicular to the nodal ring axis, $\boldsymbol{B}\|\hat{\boldsymbol{k}}_x$ as shown in Fig. 1(a), LLs form in the 2D transverse momentum plane, with k_x (parallel to the field) remaining a good quantum number. The magneto-optical conductivity sums contributions from all k_x values, capturing the distinct LLs of Dirac fermions and semi-Dirac fermions depicted in Fig. 1(c). At $k_x=0$, the Hamiltonian around zero energy is given by

$$H|_{k_x=0}\approx\hbar v_y\delta k_y\sigma_1+\hbar v_z k_z\sigma_2, \tag{3}$$

where $\delta k_y=k_y\mp k_0$ and $v_y=\hbar k_0/m$, describing (anisotropic) Dirac fermions, whereas at $k_x=\pm k_0$,

$$H|_{k_x=\pm k_0}\approx\frac{\hbar^2k_y^2}{2m}\sigma_1+\hbar v_z k_z\sigma_2, \tag{4}$$

describing semi-Dirac fermions. As the energy moves away from zero, the constant energy surfaces of the two Dirac bands located at $k_x=\pm k_0$ expand and eventually merge. At this point, the Dirac approximation is no longer applicable. As k_x shifts from zero, the energy range where the Dirac approximation is valid $[|\hbar\omega|<\hbar^2(k_0^2-k_x^2)/2m]$ narrows, leading toward the semi-Dirac regime. Note that the curved geometry of the nodal ring plays a crucial role in forming the semi-Dirac fermions, as further discussed in the conclusion. When the tilt and SOC terms are introduced, the tilt term modifies LLs without altering their scaling behavior, while the SOC term induces a gap, placing Dirac LL transitions above the SOC-induced gap. Because of the tilt-induced energy shift, semi-Dirac LL transitions remain visible even below the SOC gap. The distinction allows for clear identification of the two LL transitions, Dirac and semi-Dirac, in their respective energy ranges. These effects of the tilt and SOC are confirmed by numerical calculations (see SM, Sec. III) for the effective Hamiltonian of $SrAs_3$, including a magnetic field into Eq. (1).

Second, when the magnetic field is applied parallel to the nodal ring axis as shown in Fig. 1(b), the simplified effective Hamiltonian in the $k_z=0$ plane is given by

$$H|_{k_z=0}\approx\frac{\hbar^2}{2m}(k_x^2+k_y^2-k_0^2)\sigma_1, \tag{5}$$

which resembles those of classical electron and hole gases. The LLs inherit the properties of the classical electron (hole) gas, starting from their origin $-\varepsilon_0(\varepsilon_0)$ and increasing (decreasing) linearly with the magnetic field. Thus, the LL transitions start from $2\varepsilon_0$, the energy separation of the two gases at their origins, and decrease linearly as the LLs shift with B. As k_z deviates from zero, the second term in Eq. (2) generates a gap of $2\hbar v_z k_z$ between the two gases, resulting in reduced contributions in the low-energy range of interest. The tilt term modifies the effective masses of the electron

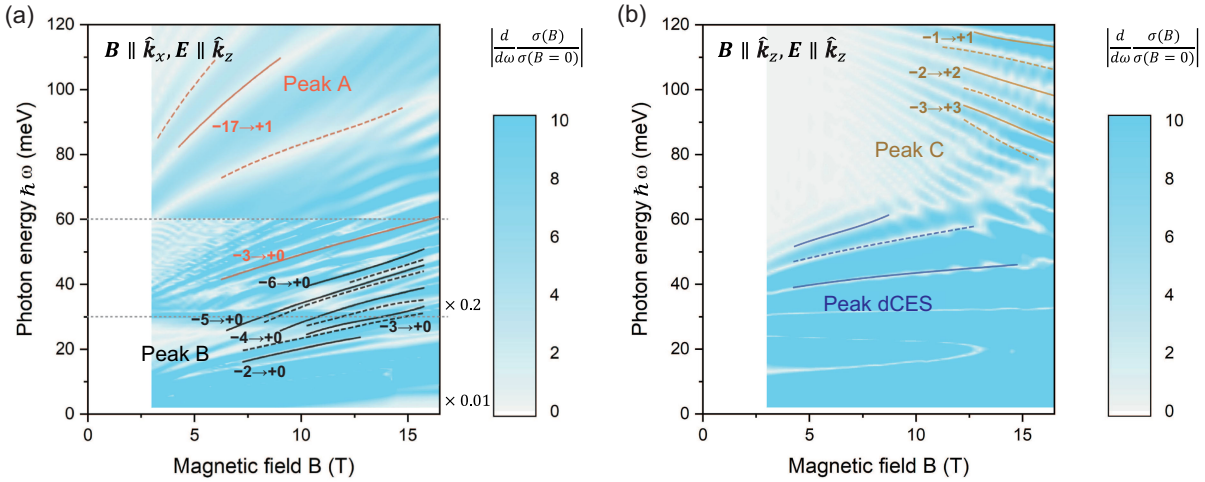

FIG. 3. Theoretical magneto-optical transition peaks calculated in the (a) $(\boldsymbol{B},\boldsymbol{E})\|(\hat{\boldsymbol{k}}_x,\hat{\boldsymbol{k}}_z)$ mode and (b) $(\boldsymbol{B},\boldsymbol{E})\|(\hat{\boldsymbol{k}}_z,\hat{\boldsymbol{k}}_z)$ mode. The derivative $|(d/d\omega)[\sigma(B)/\sigma(B=0)]|$ was employed in the 2D color plot to enhance visibility. For numerical calculations, we used the broadening term $\eta = 3$ meV except for $\hbar\omega < 60$ meV in (a) where we used the reduced $\eta = 1$ meV to identify the LL transitions of peak B beyond those experimentally measured. The color intensity was adjusted in the 30–60 meV range and < 30 meV range by multiplying the initial values by 0.2 and 0.01, respectively.

and hole gases, respectively while preserving the linear scaling of the LLs. The SOC term introduces a gap between the two gases, while its effect on the LL transitions is negligible as they occur far above this gap. Notably, the electron and hole pockets split into smaller pockets since the tilt term deforms their constant energy surfaces (CESs) into distinct ellipses, creating crossing points. In addition, the SOC term disconnects the deformed CESs around the crossing points. The disconnected CESs lead to a class of LL transitions peak dCES. See SM, Sec. IV-1 [27].

Figure 3 shows the magneto-optical conductivity obtained from the theoretical calculations for the effective Hamiltonian of $SrAs_3$, including a magnetic field into Eq. (1). The LL transitions of peaks A and B are observed in the $(\boldsymbol{B},\boldsymbol{E})\|(\hat{\boldsymbol{k}}_x,\hat{\boldsymbol{k}}_z)$ mode, whereas those of peak C and peak dCES appear in the $(\boldsymbol{B},\boldsymbol{E})\|(\hat{\boldsymbol{k}}_z,\hat{\boldsymbol{k}}_z)$ mode, with the respective energy ranges also in agreement with the experimental results. Based on this agreement, we extract the LLs responsible for the four classes of LL transition peaks, considering the effects of the tilt and SOC terms.

Figure 4 presents the relationship between the extracted LL energies and magnetic field strength, using a logarithmic plot to highlight their scaling behaviors, in both the experimental and numerical data. In Figs. 4(a) and 4(b), with the magnetic field applied perpendicular to the nodal ring axis, $\boldsymbol{B}\|\hat{\boldsymbol{k}}_x$, the LL energies exhibit the slope of $1/2$ (extracted from peak A) and $2/3$ (peak B), corresponding to Dirac and semi-Dirac fermions, respectively. In Fig. 4(c), with the field applied parallel to the nodal ring axis, $\boldsymbol{B}\|\hat{\boldsymbol{k}}_z$, the LLs exhibit the slope of 1 (peak C) aligning with classical fermions. The experimental and numerical results consistently demonstrate that the LLs represent the three types of fermions, Dirac, semi-Dirac, and classical fermions. The LLs extracted from peak dCES deviate from the simple scaling behaviors due to complex band dispersions of the disconnected electron and hole pocket. The derivation of LLs from the LL transition peaks is described in SM, Sec. IV [27].

To this point, we focused on the results of the two $(\boldsymbol{B},\boldsymbol{E})$ modes with $\boldsymbol{E}\|\hat{\boldsymbol{k}}_z$ polarization. For the other polarization $\boldsymbol{E}\|\hat{\boldsymbol{k}}_x$, the LLs exhibit the same scaling behaviors as in $\boldsymbol{E}\|\hat{\boldsymbol{k}}_z$, while the corresponding LL transitions are notably weaker in the peaks' intensities, especially for peak B and

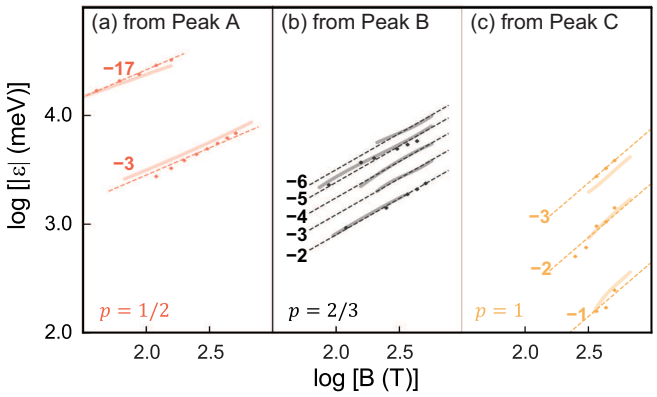

FIG. 4. Logarithmic plots of LL energies as a function of magnetic field strength extracted from (a) peak A, (b) peak B, and (c) peak C, with the respective LL indices indicated. Filled circles and shaded lines represent experimental and theoretical results, respectively. Dashed lines guide the slopes of (a) $1/2$, (b) $2/3$, and (c) 1, corresponding to Dirac, semi-Dirac, and classical fermions, respectively. The slight deviation from $1/2$ for $n = -3$ in (a) arises from mixing between the Dirac and semi-Dirac peaks, as explained in detail in SM, Sec. IV.

peak C, since the corresponding effective velocity v_x diminishes. See SM, Sec. V [27]. These findings demonstrate that an axis-resolved study is essential for a comprehensive understanding of the LL transitions of the nodal ring.

To conclude, we identified the complete, direction-resolved LL transitions of $SrAs_3$ through magneto-optical measurements. The four kinds of $(\boldsymbol{B},\boldsymbol{E})$ measurement modes, enabled by the unique single nodal ring structure, were critical in revealing them. The LL transitions elucidated two key properties of the nodal ring: first, the nodal ring hosts three distinct types of fermions simultaneously—Dirac, semi-Dirac, and classical fermions—distinguishing it from nodal point or line structures which typically exhibit only one or two fermion types. See SM, Sec. VI [27]. Their coexistence results from the unique geometry of the nodal ring, which, as shown in Fig. 1, supports linear, linear + quadratic, and quadratic energy dispersions within a single structure. The three types of fermions are well separated from each other in their excitation energies and/or in the $(\boldsymbol{B},\boldsymbol{E})$ configurations as demonstrated in Fig. 4, providing an opportunity to experimentally probe and compare their properties within the same material. Second, the curved geometry of the nodal ring ensures the emergence of the semi-Dirac fermions. When the momentum plane perpendicular to the $\boldsymbol{B}$ field becomes tangent to the nodal line (the plane II in Fig. 1), the linear dispersion along the nodal-line direction vanishes, and the next-leading quadratic dispersion becomes dominant. As a result, a semi-Dirac dispersion appears with the quadratic dispersion along the nodal-line direction and the linear dispersion along the perpendicular direction. This mechanism can be generalized to systems with a curved nodal line, for example, ZrSiS, which was recently reported to exhibit $\hbar\omega \sim B^{2/3}$ [22]. Here, semi-Dirac fermions arise at the crossing point of the nodal lines, where the curved nodal line is tangent to the momentum plane perpendicular to the $\boldsymbol{B}$ field. In the case of $SrAs_3$, which hosts a single nodal ring, semi-Dirac fermions can be accessed for any orientation of $\boldsymbol{B}$, as long as $\boldsymbol{B}$ lies within the nodal ring plane, facilitating experimental feasibility that is not achieved in other nodal-line semimetals with a complex cagelike structure. The semi-Dirac fermions bridge the gap between Dirac and classical fermions, serving as an intermediary state as demonstrated by their LL scaling power $(2/3)$ lying between $1/2$ (Dirac) and 1 (classical). The ease of access to semi-Dirac fermions provides a framework for experimentally investigating diverse quantum properties beyond the unique LL scaling behavior. Overall, our findings in $SrAs_3$ establish that a nodal ring serves as a valuable platform for advancing the understanding of topological semimetals.

Acknowledgments—The work at UOS was supported by the National Research Foundation of Korea (NRF) grant funded by the Korea government (Grant No. 2021R1A2C1009073). The work at SNU was supported by the NRF grant funded by the Korea government (Ministry of Science and ICT, MSIT) (Grant No. RS-2023-NR076715), the Creative-Pioneering Researchers Program through Seoul National University (SNU), and the Center for Theoretical Physics. The work at POSTECH was supported by the Institute for Basic Science (No. IBS-R014-D1), by the NRF of Korea government through the Basic Science Research Program (Grant No. NRF-2022R1A2C3009731), and the Max Planck POSTECH/Korea Research Initiative (Grant No. 2022M3H4A1A04074153). The N. H. M. F. L. is supported by NSF through NSF/DMR-2128556 and the State of Florida.

Data availability—The data that support the findings of this Letter are openly available [36].

[1] N. P. Armitage, E. J. Mele, and A. Vishwanath, Rev. Mod. Phys. **90**, 015001 (2018).
[2] B. Q. Lv, T. Qian, and H. Ding, Rev. Mod. Phys. **93**, 025002 (2021).
[3] A. Sekine and K. Nomura, J. Appl. Phys. **129**, 141101 (2021).
[4] H. Kim, J. M. Ok, S. Cha, B. G. Jang, C. I. Kwon, Y. Kohama, K. Kindo, W. J. Cho, E. S. Choi, Y. J. Jo, W. Kang, J. H. Shim, K. S. Kim, and J. S. Kim, Nat. Commun. **13**, 7188 (2022).
[5] M. M. Hosen, G. Dhakal, B. Wang, N. Poudel, K. Dimitri, F. Kabir, C. Sims, S. Regmi, K. Gofryk, D. Kaczorowski, A. Bansil, and M. Neupane, Sci. Rep. **10**, 2776 (2020).
[6] W. B. Rui, Y. X. Zhao, and A. P. Schnyder, Phys. Rev. B **97**, 161113(R) (2018).
[7] G.-Q. Zhao, S. Li, W. B. Rui, C. M. Wang, H.-Z. Lu, and X. C. Xie, Quantum Front. **2**, 22 (2023).
[8] L. Oroszlány, B. Dóra, J. Cserti, and A. Cortijo, Phys. Rev. B **97**, 205107 (2018).
[9] H. Isobe, B.-J. Yang, A. Chubukov, J. Schmalian, and N. Nagaosa, Phys. Rev. Lett. **116**, 076803 (2016).
[10] B. Uchoa and K. Seo, Phys. Rev. B **96**, 220503(R) (2017).
[11] J. M. Link, B. N. Narozhny, E. I. Kiselev, and J. Schmalian, Phys. Rev. Lett. **120**, 196801 (2018).
[12] S. Banerjee, R. R. P. Singh, V. Pardo, and W. E. Pickett, Phys. Rev. Lett. **103**, 016402 (2009).
[13] P. Sinha, S. Murakami, and S. Basu, Phys. Rev. B **105**, 205407 (2022).
[14] F. Le Mardelé, J. Wyzula, I. Mohelsky, S. Nasrallah, M. Loh, S. Ben David, O. Toledano, D. Tolj, M. Novak, G. Eguchi, S. Paschen, N. Barišić, J. Chen, A. Kimura, M. Orlita, Z. Rukelj, A. Akrap, and D. Santos-Cottin, Phys. Rev. B **107**, L241101 (2023).
[15] M. Zhao, Z. Yan, X. Xie, Y. Yang, P. Leng, M. Ozerov, D. Yan, Y. Shi, J. Yang, F. Xiu, and S. Dong, Phys. Rev. Mater. **6**, 054204 (2022).
[16] Z. Lu, P. Hollister, M. Ozerov, S. Moon, E. D. Bauer, F. Ronning, D. Smirnov, L. Ju, and B. J. Ramshaw, Sci. Adv. **8**, eabj1076 (2022).
[17] S. Polatkan, M. O. Goerbig, J. Wyzula, R. Kemmler, L. Z. Maulana, B. A. Piot, I. Crassee, A. Akrap, C. Shekhar,

C. Felser, M. Dressel, A. V. Pronin, and M. Orlita, Phys. Rev. Lett. **124**, 176402 (2020).
[18] D. Santos-Cottin, M. Casula, L. de' Medici, F. Le Mardelé, J. Wyzula, M. Orlita, Y. Klein, A. Gauzzi, A. Akrap, and R. P. S. M. Lobo, Phys. Rev. B **104**, L201115 (2021).
[19] Y. Shao, Z. Sun, Y. Wang, C. Xu, R. Sankar, A. J. Breindel, C. Cao, M. M. Fogler, A. J. Millis, F. Chou, Z. Li, T. Timusk, M. B. Maple, and D. N. Basov, Proc. Natl. Acad. Sci. U.S.A. **116**, 1168 (2019).
[20] Y. Shao, A. N. Rudenko, J. Hu, Z. Sun, Y. Zhu, S. Moon, A. J. Millis, S. Yuan, A. I. Lichtenstein, D. Smirnov, Z. Q. Mao, M. I. Katsnelson, and D. N. Basov, Nat. Phys. **16**, 636 (2020).
[21] E. Uykur, L. Z. Maulana, L. M. Schoop, B. V. Lotsch, M. Dressel, and A. V. Pronin, Phys. Rev. Res. **1**, 032015(R) (2019).
[22] Y. Shao, S. Moon, A. N. Rudenko, J. Wang, J. Herzog-Arbeitman, M. Ozerov, D. Graf, Z. Sun, R. Queiroz, S. H. Lee, Y. Zhu, Z. Mao, M. I. Katsnelson, B. A. Bernevig, D. Smirnov, A. J. Millis, and D. N. Basov, Phys. Rev. X **14**, 041057 (2024).
[23] S. Li, Z. Guo, D. Fu, X.-C. Pan, J. Wang, K. Ran, S. Bao, Z. Ma, Z. Cai, R. Wang, R. Yu, J. Sun, F. Song, and J. Wen, Sci. Bull. **63**, 535 (2018).
[24] Q. Xu, R. Yu, Z. Fang, X. Dai, and H. Weng, Phys. Rev. B **95**, 045136 (2017).
[25] H. Wang, Y.-X. Huang, H. Liu, X. Feng, J. Zhu, W. Wu, C. Xiao, and S. A. Yang, Phys. Rev. Lett. **132**, 056301 (2024).
[26] J. Jeon, J. Jang, H. Kim, T. Park, D. Kim, S. Moon, J. S. Kim, J. H. Shim, H. Min, and E. Choi, Phys. Rev. Lett. **131**, 236903 (2023).
[27] See Supplemental Material at http://link.aps.org/supplemental/10.1103/wfzd-7r9n for experimental details, the effective model of $SrAs_3$, analysis of the Landau levels, calculations of the magneto-optical conductivity, magneto-optical properties for $\boldsymbol{E}\|\hat{\boldsymbol{k}}_z$ mode, and comparison with previous magneto-optical experiments on topological semimetals, which includes Refs. [12,14–22,26,28–35].
[28] G. Montambaux, F. Piéchon, J.-N. Fuchs, and M. O. Goerbig, Eur. Phys. J. B **72**, 509 (2009).
[29] L. Oroszlány, B. Dóra, J. Cserti, and A. Cortijo, Phys. Rev. B **97**, 205107 (2018).
[30] H. Zhang, Y. L. Zhu, Y. Qiu, W. Tian, H. B. Cao, Z. Q. Mao, and X. Ke, Phys. Rev. B **102**, 094424 (2020).
[31] Y. Sun, H. Zhao, M. Wu, and H. Pan, Physica (Amsterdam) **599B**, 412478 (2020).
[32] D. Asafov and I. Pavlov, Phys. Rev. B **110**, 125126 (2024).
[33] S. Tchoumakov, M. Civelli, and M. O. Goerbig, Phys. Rev. Lett. **117**, 086402 (2016).
[34] Z.-M. Yu, Y. Yao, and S. A. Yang, Phys. Rev. Lett. **117**, 077202 (2016).
[35] J. Wyzula, X. Lu, D. Santos-Cottin, D. K. Mukherjee, I. Mohelský, F. Le Mardelé, J. Novák, M. Novak, R. Sankar, Y. Krupko, B. A. Piot, W.-L. Lee, A. Akrap, M. Potemski, M. O. Goerbig, and M. Orlita, Adv. Sci. **9**, 2105720 (2022).
[36] J. Jeon, T. Kim, J. Jang, H. Kim, M. Ozerov, J. S. Kim, H. Min, and E. Choi, zenodo (2025), 10.5281/zenodo.16348020.